

On the sensitivity of the diffusion MRI signal to brain activity in response to a motor cortex paradigm

A. De Luca¹, L. Schlaffke², J.C.W. Siero^{3,4}, M. Froeling³, A. Leemans¹

¹Image Sciences Institute, UMC Utrecht, Utrecht, The Netherlands

²Department of Neurology, BG-University Hospital Bergmannsheil, Ruhr-University Bochum, Bochum, Germany

³Department of Radiology, UMC Utrecht, Utrecht, The Netherlands

⁴Spinoza Centre for Neuroimaging, Amsterdam, The Netherlands

Word count: 5202

Corresponding Author:

Alberto De Luca

Heidelberglaan 100, 3584CX, Utrecht, The Netherlands

alberto@isi.uu.nl

Highlights:

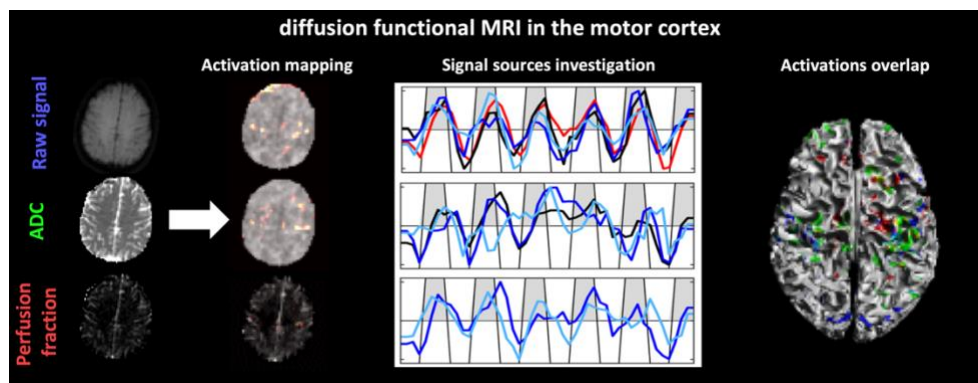
- We propose a multiple diffusion weightings scheme for diffusion functional MRI;
- The measured signal exhibits sensitivity to brain activity in the motor cortex;
- Simultaneous signal changes take place in the cellular and perfusion compartments;
- The sensitivity of the diffusion MRI signal to task is similar to that of gradient echo fMRI;

Keywords: diffusion MRI, functional MRI, activation mapping, BOLD, free water, perfusion

Abbreviations: MRI: magnetic resonance imaging; dMRI: diffusion MRI; dfMRI: diffusion functional MRI; ADC: apparent diffusion coefficient; ADC-fMRI: ADC based functional MRI; IVIM: intra-voxel incoherent motion; IVIM-fMRI: IVIM based functional MRI; GE-BOLD: gradient-echo blood oxygenation level dependent; AC: activation core;

Conflicts of interest: none

Graphical abstract



Abstract

Diffusion functional MRI (dfMRI) is a promising technique to map functional activated areas with higher spatial accuracy than classic functional MRI approaches. However, it remains unclear whether dfMRI measures changes in the cellular environment, in perfusion and/or in T_2 values. We designed an acquisition/quantification scheme to disentangle such effects in the motor cortex during a finger tapping paradigm. dfMRI was acquired at specific diffusion weightings to selectively suppress perfusion and free-water diffusion, then times series of the apparent diffusion coefficient (ADC-fMRI) and of the perfusion signal fraction (IVIM-fMRI) were derived. ADC-fMRI provided ADC estimates sensitive to perfusion and free-water volume changes, but not to T_2 and T_2^* changes. With IVIM-fMRI we isolated the perfusion contribution to ADC, while suppressing T_2 effects. Compared to conventional fMRI, activation maps obtained with dfMRI and ADC-fMRI had smaller clusters with a spatial overlap between the three techniques below 50%. Increases of perfusion fractions were observed in correspondence of task execution in both dfMRI and ADC-fMRI activations. Perfusion effects were more prominent with ADC-fMRI than with dfMRI but were significant in less than 25% of activation ROIs. Taken together, our results suggest that the sensitivity of dfMRI goes beyond pure perfusion changes and support previous evidence on its higher spatial accuracy compared to classic functional MRI.

Introduction

Diffusion MRI (dMRI) is a non-invasive in vivo technique sensitive to the displacement of water molecules. Despite the dynamic nature of the signal, dMRI is mostly regarded as a structural technique providing static and reproducible snapshots of the imaged tissue (Acheson et al., 2017; Grech-Sollars et al., 2015). The dMRI signal carries information about different components of tissue microstructure. At strong diffusion weightings, the signal is mainly informative of the intra and extra-cellular environments (Winston, 2012), whereas at low diffusion weightings, it is sensitive to intra-voxel incoherent motion (IVIM) phenomena, including perfusion (Le Bihan et al., 1988) and free water diffusion (Pasternak et al., 2009; Pierpaoli and Jones, 2004). In the brain, the IVIM model has been used to quantify perfusion changes during CO₂ challenges (Federau et al., 2012), or in presence of disease (Iima and Le Bihan, 2016) as cancer (Keil et al., 2017). The concept of IVIM and its applications suggest sensitivity of the dMRI signal acquired at low (i.e., $b \leq 200$ s/mm²) to moderate b-values (i.e., $b \leq 500$ s/mm²) to physiological dynamics in the vascular and free-water pools. Such sensitivity applies also to the non-diffusion weighted images, which are the reference images for most diffusion experiments.

At strong diffusion weightings (i.e., $b \geq 1000$ s/mm²), the dMRI signal measured in the brain originates mainly from cellular components, where structure and not function is assumed to be fairly constant over short time spans. In other words, if dMRI is assumed to be insensitive to function, it is also reasonable to consider that it is static, implying that the signal should not change over time beyond experimental noise. Nevertheless, an increasing number of reports is challenging the static nature of dMRI at strong diffusion weightings in the brain. Darquié and colleagues (Darquié et al., 2001) originally observed that visual stimuli administered during a dMRI experiment caused small but reproducible alterations of the apparent diffusion coefficient (ADC). In their experiment, the authors repeatedly acquired data at both low ($b = 200$ s/mm²) and strong diffusion weightings ($b = 1400$ s/mm²). In a later experiment, which included more diffusion weightings (Le Bihan et al., 2006), the authors proposed a bi-exponential formulation based on a slow and fast pool model, and observed a 1.7% expansion of the slower diffusion pool during visual stimuli. In the conclusions of their work, cell swelling after neuronal firing was proposed as an explanation of the findings. Other reports have independently confirmed the potential of diffusion functional MRI (dfMRI) in terms of improved spatial localization of brain activations as compared to standard gradient-echo fMRI (GE-BOLD) (Song et al., 2002), and showed that it well represents underlying neuronal activity in rats (Nunes et al., 2019). Furthermore, the response function (RF) of the dfMRI signal, a mathematical description that relates the stimulation paradigm to signal changes, has been suggested to have a shorter time to peak compared to GE-BOLD (Aso et al., 2009), which can be considered to be supporting the neuronal firing theory.

Despite these promising reports, most of the mechanisms of dfMRI, as well as its feasibility and usefulness, are yet to be investigated. Miller et al. (Miller et al., 2007) challenged the neuronal firing theory, suggesting a major role of the “ T_2 shine through” effect (Provenzale et al., 1999) on the dfMRI signal. Furthermore, acquisition protocols and processing approaches are far from established, as previous studies used either low (Song et al., 2002) or strong diffusion weightings (Darquié et al., 2001; Le Bihan et al., 2006; Nicolas et al., 2017; Williams et al., 2014), with limited evidence beyond the visual cortex (Song et al., 2002).

In this work, we investigated whether the dfMRI signal measured at increasing diffusion weightings, and the derived apparent diffusion coefficient (ADC) fMRI (ADC-fMRI), and intra-voxel incoherent motion fMRI (IVIM-fMRI) signals, are sensitive to brain activations in response to a finger tapping paradigm. Under specific hypothesis on the different sensitivity of dfMRI, ADC-fMRI and IVIM-fMRI to physiological changes (see Methods section), we compared their responses to task in the motor cortex to investigate alterations in cellular diffusivity, perfusion volume and T_2 value.

Methods

In this study we performed fMRI acquisitions while eliciting brain activations in the motor cortex with a finger-tapping task (Akhlaghi et al., 2012). Being well studied, straightforward to implement, and consisting of only two conditions (rest vs task), this paradigm represented an excellent starting point for the investigation of the dfMRI signal in the motor cortex.

Dataset

Seven subjects (24 ± 3 years, 4 females) underwent a 3T MRI session. The experiment was approved by the local ethical committee, and informed written consent was obtained from all subjects.

MRI acquisition

Data were acquired on a research dedicated Philips Ingenia CX scanner (Philips Medical System NV) with multi-band (MB) imaging capabilities (Setsompop et al., 2012) and a 32ch head coil. The acquisition protocol consisted of anatomical T_1 -weighted imaging, a GE-BOLD, and two dfMRI acquisitions. The second dfMRI run of one subject was not completed due to time constraints.

The main imaging parameters of each sequence are reported in Table 1.

| Sequence | Resolution (mm ³) | MB | SENSE | TE (ms) | TR (ms) | Slices | FOV (mm) | b-values (s/mm ²) | Duration |
|----------|----------------------------------|----|-------|------------|------------|--------|-----------------|----------------------------------|----------|
| T_1 -w | 1x1x1 | - | 2+2.6 | 3.7 | 8 | 180 | 256x256 x180 | - | 3m54s |
| GE-BOLD | 2.5x2.5x3 | 2 | 2 | 30 | 2000 | 52 | 240x240 x156 | - | 6m40s |
| dfMRI 1 | 2.5x2.5x4 | 2 | 2 | 96 | 8000 | 14 | 240x240 x56 | 0,300,800 | 6m50s |
| dfMRI 2 | 2.5x2.5x4 | 2 | 2 | 96 | 8000 | 14 | 240x240 x56 | 0,300,1200 | 6m50s |

Table 1 – Imaging parameters of the sequences employed in this study. No slice gap was employed for any of the sequences. Data at $b = 300, 800, 1200$ s/mm² were acquired with gradients along three orthogonal directions aligned with the scanner axes. MB: multi-band; SENSE: sensitivity encoding parallel imaging acceleration; TE: echo time; TR: repetition time; FOV: field of view.

Functional acquisitions

To elicit motor activation, we implemented a previously reported experiment design (Nicolas et al., 2017), which alternates six repetitions of rest and activation blocks with 32 seconds duration (384 s in total). Instructions were presented on a video device installed in the MR scanner room, and the start condition (task or rest) was pseudo-randomized across subjects (5 subjects started with task blocks,

whereas 2 with rest blocks). Three functional datasets were acquired for each subject. The first acquisition was a GE-BOLD sequence featuring 16 dynamics repeated over six task and six rest blocks, for a total of 192 volumes. The second and the third acquisitions were dfMRI sequences with four dynamics per diffusion weighting, repeated in six task and six rest blocks, for a total of 48 volumes per diffusion weighting. The acquisition of multiple diffusion weightings resulted in less dynamics per block compared to a GE-BOLD acquisition. However, with these data we can investigate different microstructural components, as explained in the following section.

Separating physiological contributions with dfMRI, ADC-fMRI and IVIM-fMRI

The GE-BOLD signal is T_2^* weighted, hence it reflects changes in both blood volume and oxygenation. For this reason, the GE-BOLD signal is highly sensitive to metabolic changes, but it is not specific. The dfMRI images are sensitive to changes in T_2 and in the volume of its signal compartments, i.e., the vasculature, intra- and extra-cellular water, and free water. The normalized signal S measured at time t_j , echo time T_E , and diffusion weighting b , can be expressed as:

$$S(t_j) = \sum_i f_i e^{-\frac{T_E}{T_{2,i}(t_j)}} e^{-bD_i(t_j)},$$

where f_i is the signal fraction, $T_{2,i}$ the T_2 value, and D_i the diffusion coefficient of the i -th component. Adjusting the diffusion weighting in the dfMRI experiment allows one to selectively suppress specific contributions. Data acquired at $b = 0 \text{ s/mm}^2$ are sensitive to all tissue components, whereas data at $b = 300 \text{ s/mm}^2$ are considered free of contributions from large vessels (e.g. signal change $< 5\%$ for spins diffusing faster than $10 \times 10^{-3} \text{ mm}^2/\text{s}$) (Federau et al., 2015; Finkenstaedt et al., 2017; H. et al., 2011). At stronger diffusion weightings, as $b = 800 \text{ s/mm}^2$ and $b = 1200 \text{ s/mm}^2$, the signal is considered to be insensitive to most vascular contributions (e.g. signal change $< 5\%$ for spins diffusing faster than $3.7 \times 10^{-3} \text{ mm}^2/\text{s}$ and $2.5 \times 10^{-3} \text{ mm}^2/\text{s}$, respectively). Data acquired at $b = 1200 \text{ s/mm}^2$ are also insensitive to contributions from free water diffusion, as the dfMRI signal is attenuated by over 96% at that diffusion weighting.

If the tissue composition is mono-compartmental, i.e. $i = 1$ in the above equation, all dfMRI data are sensitive to T_2 changes independently from the applied diffusion weighting. However, if T_2 changes take place only in specific components, for instance only in the vascular network, dfMRI data acquired at $b \geq 300 \text{ s/mm}^2$ should be insensitive to such effects. In addition to the T_2 sensitivity, dfMRI is partly sensitive to T_2^* effects – and hence to venous contribution – as it relies on the echo-planar-imaging readout, but to a lesser extent than GE-BOLD (Goense and Logothetis, 2006).

If the acquired dfMRI data contains at least two diffusion weightings, it is possible to compute the apparent diffusion coefficient (ADC) over time (ADC-fMRI). ADC-fMRI is traditionally considered free

of T_2 and T_2^* sensitivity, as such dependencies cancel out in the ADC equation. However, this is only true for a mono-component tissue formulation ($i=1$). If multiple components coexist in one voxel, ADC-fMRI becomes sensitive to factors affecting the $b = 0$ s/mm² image, such as perfusion and free water volume changes, among others.

If the dfMRI experiment features three or more diffusion weightings with appropriate values, it is possible to subdivide the signal contributions into vascular and non-vascular components, applying the IVIM-fMRI model in a bi-exponential formulation ($i = 2$):

$$S = f_{IVIM}e^{-bD^*} + (1 - f_{IVIM})e^{-bMD_{IVIM}}.$$

In the above equation, f_{IVIM} represents the signal fraction of a pool including both pseudo-diffusion and free-water contributions with diffusion coefficient D^* , whereas MD_{IVIM} reflects the contributions of both intra- and extra-cellular diffusion changes. Under such assumptions, the temporal series of f_{IVIM} (in the following, referred to as f_{IVIM} -fMRI) reflects the volumes changes related to free-water/perfusion and is theoretically free of T_2 and T_2^* contamination, whereas the temporal series of MD_{IVIM} (in the following, referred to as MD_{IVIM} -fMRI) summarizes cellular-related diffusion changes.

Data pre-processing

T_1 -weighted data were processed with the standard FSL pipeline “fsl_anat” to derive tissue segmentations of grey matter (GM), white matter (WM) and cerebrospinal fluid (CSF), which were then registered to the GE-BOLD space with Elastix (Klein et al., 2010, 2007). Further, the FreeSurfer reconstruction pipeline (Dale et al., 1999) was used to derive the GM/WM interface used for the graphical representations.

GE-BOLD data of each subject was corrected for subject motion using the FSL (Jenkinson et al., 2012) tool MCFLIRT (Jenkinson et al., 2002), realigning all volumes to the first volume. Individual GE-BOLD data were used as the space of reference for all functional analyses.

The processing pipeline applied to dfMRI data is elucidated in Figure 1. The two dfMRI series were concatenated, corrected for subject motion and eddy currents using ExploreDTI (Leemans et al., 2009), and transformed to the individual fMRI space using a non-linear b-spline transformation restricted to the phase-encoding direction (Klein et al., 2010). Brain extraction was performed on the dfMRI data with FSL BET (Smith, 2002). The dMRI data corresponding to each diffusion weighting (b -value) were geometrically averaged.

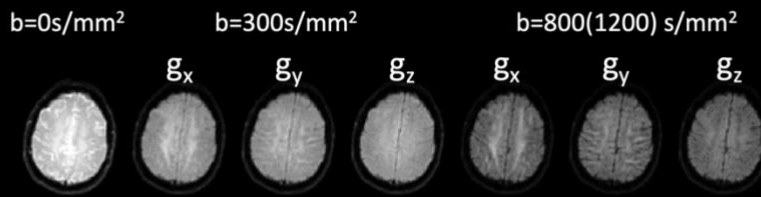
dfMRI, ADC-fMRI, IVIM-fMRI processing

We performed Z-normalization of the dfMRI data, i.e., we subtracted from each time series its average value and divided it by the standard deviation, independently for each diffusion weighting. We then concatenated the normalized data to maximize the statistical power in the subsequent analyses.

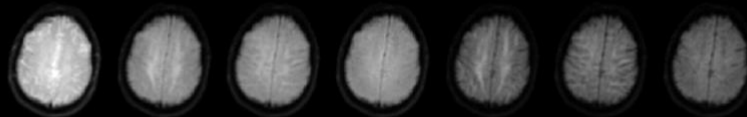
The ADC-fMRI estimates were computed by combining the data at $b = 0 \text{ s/mm}^2$ with the data at $b = 300 \text{ s/mm}^2$ (ADC-fMRI³⁰⁰), $b = 800 \text{ s/mm}^2$ (ADC-fMRI⁸⁰⁰), and $b = 1200 \text{ s/mm}^2$ (ADC-fMRI¹²⁰⁰),

Workflow of this study

dfMRI acquisition, TR=8s, 336 volumes

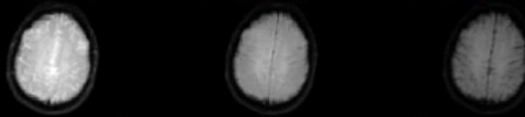


Motion correction, warping to GE-BOLD



Geometric averaging of raw signals (dfMRI)

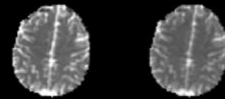
$b=0\text{s/mm}^2$ $b=300\text{s/mm}^2$ $b=800(1200)\text{s/mm}^2$



Derive temporal ADC

ADC-fMRI^{300} ADC-fMRI^{800}

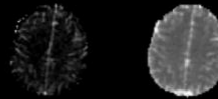
ADC-fMRI



Temporal IVIM parameters

$f_{\text{IVIM-fMRI}}$ $\text{MD}_{\text{IVIM-fMRI}}$

IVIM-fMRI



Z normalization, statistical tests (FWE + cluster correction)

$Z(\text{dfMRI})$

$Z(\text{ADC-fMRI})$

$Z(f_{\text{IVIM-fMRI}})$



Activations overlap

Temporal series in ROIs

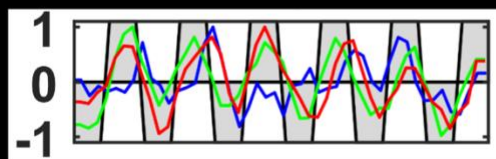


Figure 1: Workflow of this study. dfMRI data are firstly processed to attenuate motion and eddy currents related artefacts, then warped to the individual GE-BOLD space, which is used as standard space for all analysis. Data are geometrically averaged per diffusion weighting and used 1) directly for activation mapping or 2) to derive ADC-fMRI and IVIM-fMRI. After activations are individually mapped, temporal series of the signals in the activation ROIs are computed. Acronyms: $g_{x,y,z}$: diffusion gradient along the x, y or z axis; FWE: family-wise error; $TTP_{1,2}$: time-to-peak of the two Gamma functions.

separately, using the ordinary linear least-squares fit (MATLAB R2016b, The Mathworks Inc). Each ADC-fMRI series was normalized independently and then concatenated.

The IVIM-fMRI fit of the data was performed by using a bi-exponential formulation (Cho et al., 2015), and a segmented fit method (Sigmund et al., 2012). Values of perfusion fractions (f_{IVIM} -fMRI) and of the perfusion corrected mean diffusivity (MD_{IVIM} -fMRI) over time were computed for both the first (f_{IVIM} -fMRI^{300,800}, MD_{IVIM} -fMRI^{300,800}) and the second acquisition (f_{IVIM} -fMRI^{300,1200}, MD_{IVIM} -fMRI^{300,1200}). The abovementioned approaches are schematically summarized in Figure 1.

The merged Z(dfMRI), Z(ADC-fMRI) and Z(f_{IVIM} -fMRI^{300,800}) time-series featured 288, 192, and 48 volumes, respectively.

Activation ROIs mapping

Task induced activations were mapped on the GE-BOLD data using FSL FEAT with cluster correction for multiple comparisons. The default hemodynamic response function (HRF), i.e., the convolution of the paradigm design with a gamma function (average delay 3s, standard deviation 6s) (Glover, 1999), was used to determine the voxel-wise Z-values, which were corrected for multiple comparisons using a first level Z-threshold equal to 0.5 and a cluster p-value equal to 0.05, and finally thresholded at $Z \geq 2.3$ (Nicolas et al., 2017). The statistical analysis of Z(dfMRI), Z(ADC-fMRI), Z(MD_{IVIM} -fMRI) and Z(f_{IVIM} -fMRI) was performed similarly to that of GE-BOLD but employing a box-car response function in place of the default HRF. Flat projection maps of the Z-scores of the spatial activations with GE-BOLD, dfMRI, ADC-fMRI can be found in the Supplementary Material.

Time-series in activation ROIs

Statistically significant ROIs of Z(dfMRI) and Z(ADC-fMRI) were thresholded above 70% of their peak value to determine the activation core (AC) (Nicolas et al., 2017), here defined as AC(dfMRI) and AC(ADC-fMRI). dfMRI at each diffusion weighting, ADC-fMRI and GE-BOLD were corrected for linear trends, Z-normalized, spatially averaged within the AC ROIs and temporally processed with a three-points moving average filter, to mitigate high frequency noise and divided by their maximum value. The same analysis was repeated using the whole GM, WM and CSF masks as ROIs, to ensure changes

observed in the time-series were activation specific and not global. Results of this step can be found in the Supplementary Material.

Further, the Z-scores of the average GE-BOLD, dfMRI and ADC-fMRI signals of each subject were overlaid to investigate the sensitivity of the signals to task, as well as to qualitatively observe temporal aspects – e.g. lags in their response.

Relative percent changes of dfMRI, ADC-fMRI and f_{IVIM} -fMRI between the task and rest conditions were derived for each subject. The signals were averaged within the ROIs and over time within the corresponding blocks, then statistical significance was assessed with Z-tests.

Spatial overlap of activation ROIs

The spatial agreement between two spatial activation maps, referred as A and B, was quantified using the overlap metric, which is defined as:

$$\text{OVERLAP}(A, B) = \frac{|A \cap B|}{\min(|A|, |B|)},$$

with the operator $|A|$ indicating the volume of A.

Comparisons were performed between GE-BOLD, dfMRI and ADC-fMRI. Furthermore, the effect of perfusion on dfMRI and ADC-fMRI was quantified computing their overlap with f_{IVIM} -fMRI activations. Finally, projection maps of the Z-scores of the overlaps between GE-BOLD, dfMRI and ADC-fMRI were computed by summing their values along the z-axis, to qualitatively appreciate their extents in a planar format. These maps can be found in the Supplementary Material.

Results

dfMRI

Figure 2 shows the 3D mapping on the WM/GM interface of the activations detected in correspondence of the task > rest condition with dfMRI, GE-BOLD and their overlap. Bilateral activation in the primary motor cortex area is observed on the dfMRI activation maps of all subjects, whereas the supplementary motor area is detected only on 2 out of 7 subjects. The activation maps with dfMRI include some artefactual patterns and have smaller activation clusters than those with GE-BOLD. The overlap between statistically significant voxels of dfMRI and GE-BOLD is $42 \pm 17\%$. Axial projections of the activation maps and of the spatial overlap are shown in Supplementary Figure S2.

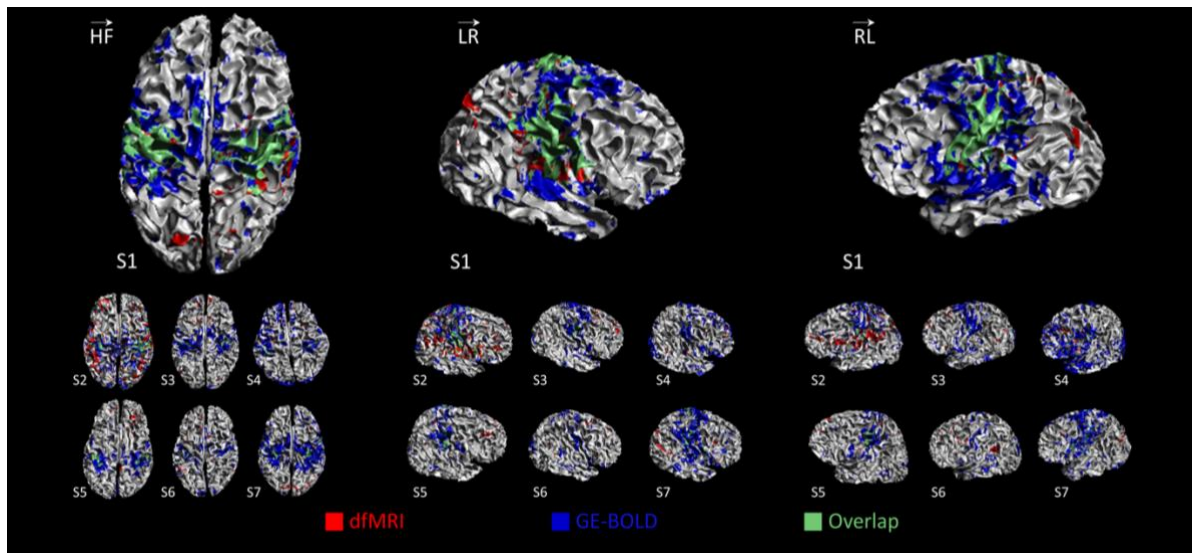


Figure 2: dfMRI vs GE-BOLD activation maps. Individual activation maps detected with dfMRI (red) as compared to GE-BOLD (blue), and their overlap (green) overlaid on the grey/white matter surface of each subject. Bilateral activation as response to finger tapping was observed on all subjects with both sequences. Activations with dfMRI were smaller than those with GE-BOLD. Spurious activations due to multi-band reconstruction artefacts can be spotted on the dfMRI activations of some subjects.

Time-series of GE-BOLD, dfMRI (for different diffusion weightings), MD_{IVIM} -fMRI and f_{IVIM} -fMRI averaged within AC(dfMRI) are reported in Figure 3. All diffusion weighted signals consistently show increases in correspondence of task execution followed by decreases at rest, similarly to GE-BOLD. Although all signal changes are consistent with the task-rest paradigm, signals acquired at $b = 800, 1200 \text{ s/mm}^2$ exhibit a larger number of artefacts than those at $b = 300 \text{ s/mm}^2$. Considering the average signals within task and rest blocks, we observe significant increases of $0.64 \pm 0.23\%$ ($p=10^{-4}$), $0.37 \pm 0.16\%$ ($p = 10^{-3}$), $0.35 \pm 0.13\%$ ($p = 10^{-3}$) and $0.53 \pm 0.24\%$ ($p = 10^{-3}$) during the task for $b = 0, 300, 800,$ and 1200 s/mm^2 , respectively.

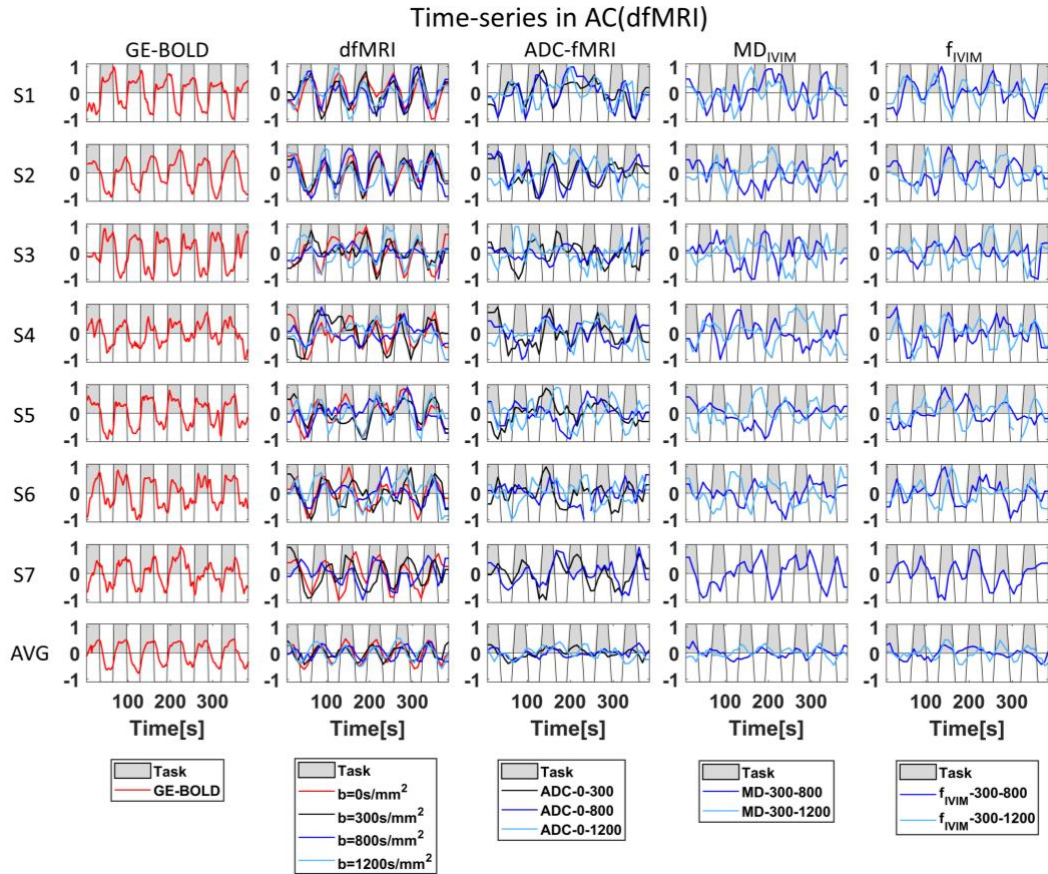


Figure 3: Time-series in AC(dfMRI). Normalized average time-series of GE-BOLD, dfMRI (for different diffusion weightings, red, black, blue and light blue solid lines), ADC-fMRI, MD_{IVIM} and f_{IVIM} of each subject (each row), and after group averaging (last row), within the dfMRI activation ROIs. Grey blocks correspond to task execution, whereas white blocks to rest. GE-BOLD and dfMRI showed increases and decreases in correspondence of task and rest, respectively. f_{IVIM} showed synchronization with the task execution, but to a less extent than dfMRI. The MD_{IVIM} signal was characterized by strong pseudo-random fluctuations, but its average variation suggested its decrease during task execution.

Normalized time-series computed using the whole GM, WM and CSF segmentations, which are shown in Supplementary Figure S1, do not show any consistency with the task-rest paradigm. MD_{IVIM} -fMRI and f_{IVIM} -fMRI are very noisy at individual levels, but on average showed response to task execution, with f_{IVIM} -fMRI³⁰⁰⁻⁸⁰⁰ showing an increase between 4 and 5%, and MD_{IVIM} -fMRI a decrease during finger tapping. The average changes of the considered metrics from task to rest within AC(dfMRI), and their statistical significance, are reported in Supplementary Information Table S1.

Activations detected with f_{IVIM} -fMRI appear noisier than those with dfMRI and characterized by smaller spatial extents. The overlap between activations from the two techniques is limited, equal to $15 \pm 12\%$.

Figure 4 shows the Z-score of the time-series of GE-BOLD and dfMRI at multiple diffusion weightings. The sensitivity of the dfMRI signal to task was similar to that of GE-BOLD, with increases and decreases

reaching ± 2 standard deviations of the signal. Considering the average inter-subject signals, changes in dfMRI at $b = 1200 \text{ s/mm}^2$ slightly anticipated those at $b = 0 \text{ s/mm}^2$.

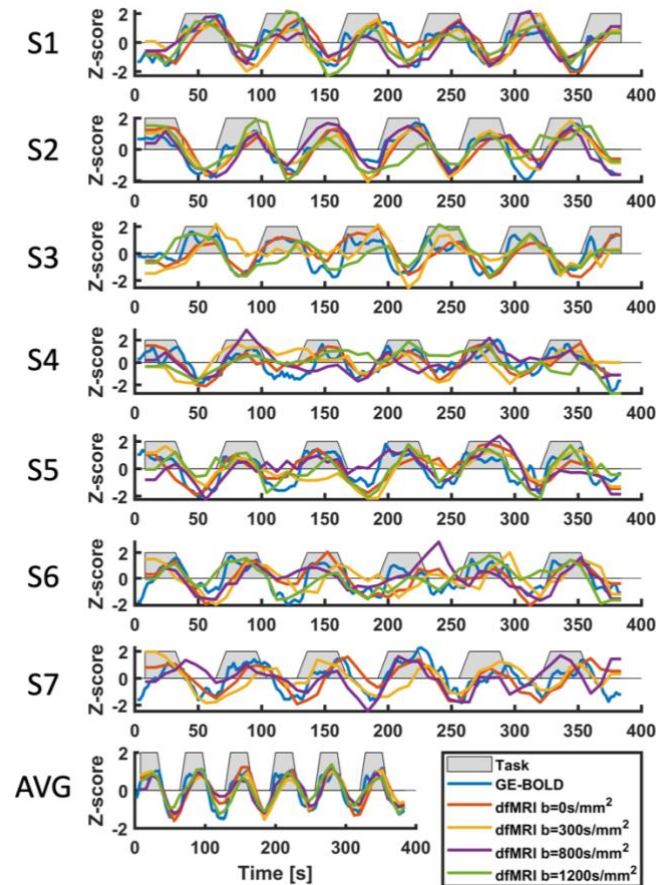


Figure 4: Sensitivity of GE-BOLD and dfMRI in AC(dfMRI). Z-score of the time-series of GE-BOLD and dfMRI (for different diffusion weightings, red, orange, purple solid lines) within the dfMRI activation core. The individual dfMRI signals showed signal changes up to 2 standard deviations in correspondence of task execution in line with GE-BOLD, irrespectively of the applied diffusion-weighting. The time-series suggest that dfMRI signals at $b=1200 \text{ s/mm}^2$ exhibited slightly faster reactivity to task than data at $b=0 \text{ s/mm}^2$, whereas differences with GE-BOLD were minimal.

ADC-fMRI

Figure 5 shows a 3D rendering of the functional activation maps detected with ADC-fMRI, GE-BOLD and their overlap on the GM/WM interface. Bilateral activations in the primary motor cortex are observed on all subjects with ADC-fMRI, but they have a smaller extension than those observed with dfMRI. Furthermore, activations with ADC-fMRI appear noisier compared to dfMRI. The overlap between $Z(\text{ADC-fMRI})$ and GE-BOLD is $35 \pm 13\%$, while the overlap between $Z(\text{ADC-fMRI})$ and $Z(\text{dfMRI})$ is the lowest, $18 \pm 8\%$. Axial projections of the activation maps of ADC-fMRI and of its spatial overlap with dfMRI and GE-BOLD are shown in Supplementary Figure S2.

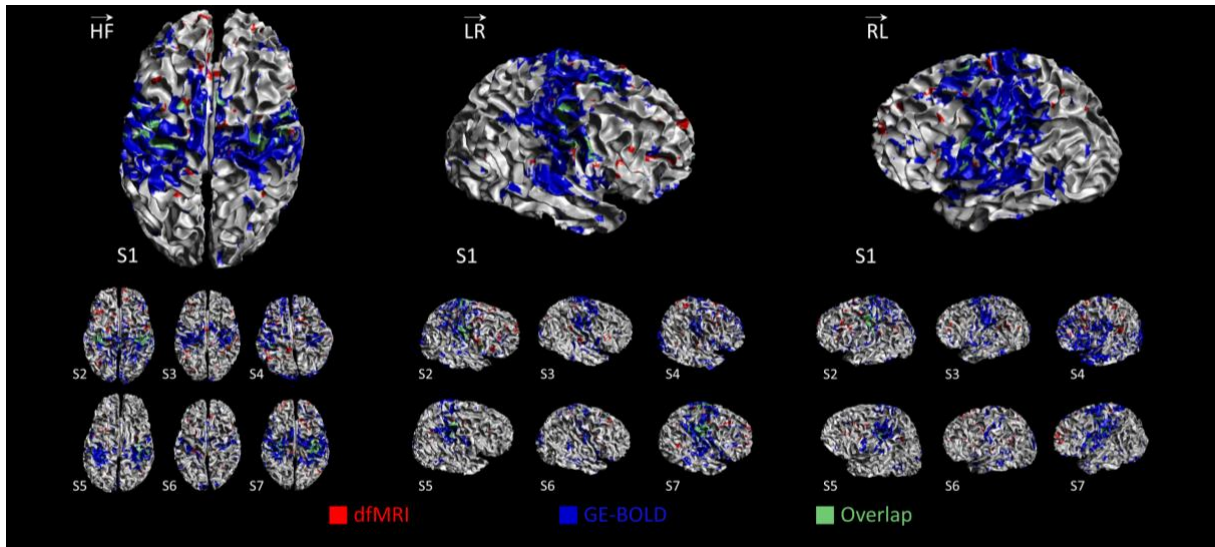


Figure 5: ADC-fMRI vs GE-BOLD activations maps. Individual activation maps detected with ADC-fMRI (red) as compared to GE-BOLD (blue), and their overlap (green) overlaid on the grey/white matter surface of each subject. Bilateral activation was observed on all subjects with both sequences. However, activations with ADC-fMRI were weaker than those with dfMRI, and generally did not include the supplementary motor cortex. Compared to GE-BOLD, activations from Z(ADC-fMRI) had smaller extension.

Time-series of GE-BOLD, ADC-fMRI, MD_{IVIM} -fMRI and f_{IVIM} -fMRI within AC(ADC-fMRI) are shown in Figure 6. The average GE-BOLD signal follows the task-rest paradigm, but to a smaller extent than in the dfMRI activations. Changes of Z(ADC-fMRI) are highly coherent with the functional paradigm, with an increase during task followed by a decrease at rest. The first run of subject S3 does not show such behaviour due to a signal discontinuity artefact approximately at the half of the acquisition. During task, significantly higher ADC values than at rest are observed, $3.26 \pm 1.88\%$ for ADC-fMRI³⁰⁰ ($p = 10^{-3}$), $1.23 \pm 0.58\%$ for ADC-fMRI⁸⁰⁰ ($p = 10^{-3}$), and $1.50 \pm 0.91\%$ ($p = 10^{-2}$) for ADC-fMRI¹²⁰⁰. The average changes of the considered metrics from task to rest within AC(ADC-fMRI), and their statistical significance, are reported in Supplementary Information Table S2.

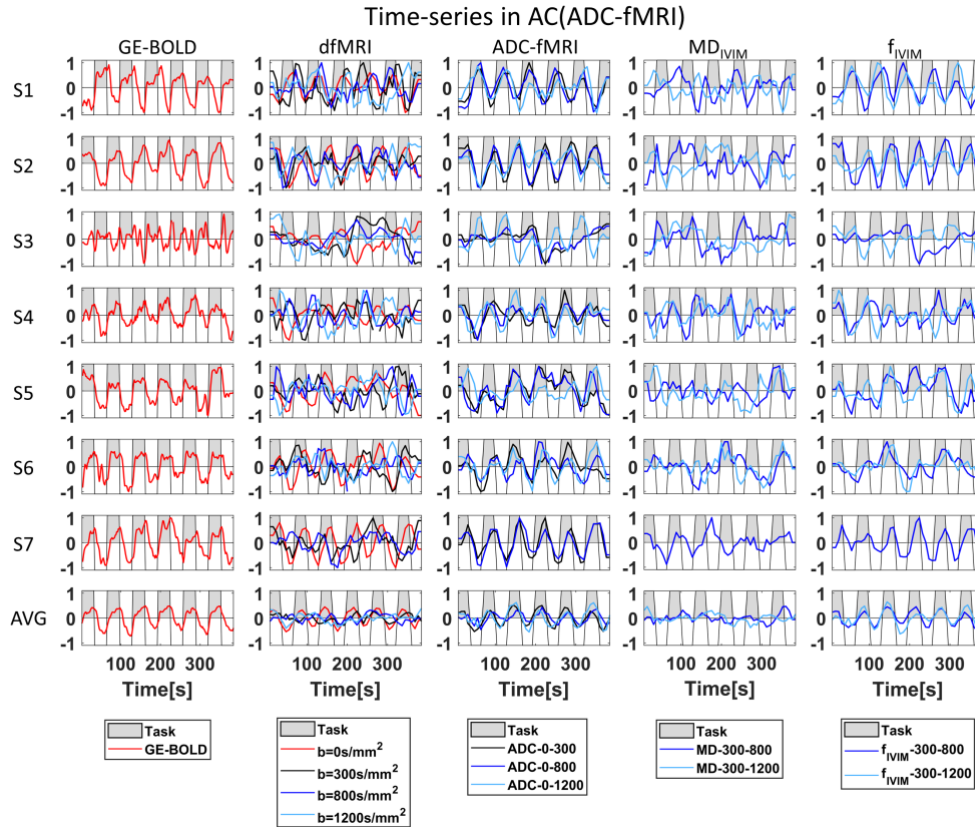


Figure 6: Time-series in AC(ADC-fMRI). Normalized average time-series of GE-BOLD, dfMRI (for different diffusion weightings, ADC-fMRI, MD_{IVIM} and f_{IVIM} of each subject (each row), and after group averaging (last row), within the ADC-fMRI activation ROIs. Grey blocks correspond to task execution, whereas white blocks to rest. GE-BOLD and ADC-fMRI showed increases and decreases in correspondence of task and rest, respectively. f_{IVIM} increases with task execution and decreases during rest were more prominent within ADC-fMRI activations than within AC(dfMRI). The average of the MD_{IVIM} signal did not exhibit clear correlations to the task.

Within the AC(ADC-fMRI) ROIs, $f_{IVIM}\text{-fMRI}^{300-800}$ shows a strong dependence on task execution and shows an increase of on average around 12% during activation compared to rest. However, the overlap between ADC-fMRI activations and $f_{IVIM}\text{-fMRI}^{300-800}$ activations is relatively modest, $22\pm 12\%$. No correlation between MD_{IVIM}-fMRI and task execution is observed within AC(ADC-fMRI).

Figure 7 shows the Z-score of the time-series of GE-BOLD and ADC-fMRI computed with three different combinations of diffusion weightings. The ADC-fMRI series showed signals increases and decreases up to ± 2 standard deviations, but its changes exhibited a consistent higher delay with task execution compared to GE-BOLD and dfMRI (Figure 4).

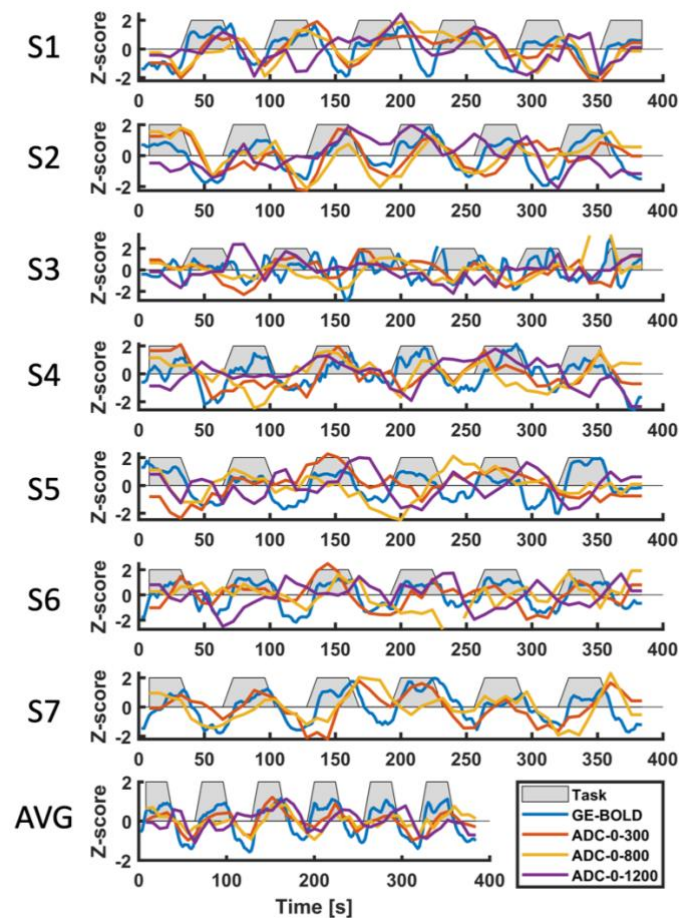


Figure 7: Sensitivity of GE-BOLD and ADC-fMRI in AC(ADC-fMRI). Z-score of the time-series of GE-BOLD and ADC-fMRI within the ADC-fMRI activation core. The individual ADC-fMRI signals showed signal changes up to 2 standard deviations in correspondence of task execution in line with GE-BOLD, irrespectively of the applied diffusion-weighting. The time-series suggest that ADC-fMRI signals have higher delay to task execution than GE-BOLD.

Discussion

In this work, we investigated changes in the diffusion-weighted signal measured in the brain during a motor cortex paradigm to verify whether i) the dMRI signal acquired at different diffusion weightings is sensitive to functionality in motor involved areas; and ii) it is possible to separate the signal sources from the observed dfMRI signal changes. Our findings suggest that the dMRI signal is sensitive to brain functionality, and that perfusion/free-water changes can explain only part of the observed signal alterations.

Clusters where the paradigm significantly explained the dfMRI signal were detected in all subjects. The activations detected with dfMRI (Figure 2) are located approximately in the same areas as observed

with GE-BOLD, but their extension is remarkably smaller, in line with a previous study on the visual cortex (Nicolas et al., 2017). Furthermore, the overlap between the activations from the two techniques is limited, with values smaller than 50%, suggesting adjacent and only partially overlapping areas. The reduced extension can be explained either by an SNR deficit in the dfMRI data, or by choice of the box-car response function in place of a more sophisticated formulation (Aso et al., 2009), or by considering the crushing effect of the diffusion gradients on the vascular network, which is likely to reduce the activation extent leading to a more accurate spatial localization, as previously suggested (Song et al., 2002).

The time-series reported in Figure 3 show remarkable synchronization between task execution and dfMRI signal changes at different diffusion weightings. Although the observed alterations are modest in absolute value, i.e., below 1%, they are reproducible across subjects, and statistically significant ($10^{-4} < p < 10^{-2}$). In our study, average signal changes observed at $b = 800$ and 1200 s/mm² slightly anticipated those at $b = 0$ s/mm², which is in line with previous studies (Aso et al., 2013, 2009; Le Bihan et al., 2006), although no quantitative evaluation could be performed due to TR limitations. It should also be noted that in contrast to the abovementioned studies, here we acquired two diffusion weightings (in addition to the $b = 0$ s/mm² volume) per run, which results in an intrinsic temporal offset of 1.5 seconds between different diffusion weightings, for which we did not explicitly account. While considering such shift is not trivial, this acquisition scheme offers the advantage of acquiring multiple diffusion weightings in a reasonable time and ensures that all data experience the same physiological status.

A controversial point about dfMRI relates to its underlying physiological mechanisms. Some studies suggest that these mechanisms have a neuronal (or closer to) origin (Darquié et al., 2001; Le Bihan et al., 2006; Nunes et al., 2019), whereas others show a perfusion related origin (Miller et al., 2007; Rudrapatna et al., 2012). Although strong diffusion gradients (i.e., $b = 1200$ s/mm²) are expected to completely suppress the perfusion signal, this might still affect the measured signal via the “T₂ shine-through” effect (Provenzale et al., 1999). This would be especially true if the signal would originate from a single tissue component, which is not likely to be the case. Using a two-component model, we observed increases of perfusion signal fractions in AC(dfMRI), between 4 and 5%. Hypothesizing invariance of the intra/extracellular environment, such perfusion changes would result in net signal alterations at $b = 800$ and 1200 s/mm² above 1%. Taking into account that MD_{IVIM}-fMRI (Figure 3) – which is theoretically free of perfusion/T₂/T₂* contamination – shows weak but consistent decreases in AC(dfMRI) during task execution, we suggest that in such ROI a reduction of cellular diffusivity (Darquié et al., 2001) takes place simultaneously to increases in T₂ and blood volume (Miller et al., 2007). This is also consistent with the observation of slightly faster reactivity to task of the dfMRI signal at $b = 1200$ s / mm² compared to that at $b = 0$ s/mm² (Figure 4), and with our results on the overlap

between $Z(\text{dfMRI})$ and $Z(f_{\text{IVIM-fMRI}}^{300-800})$ activations, which is rather poor (around 15%), suggesting that perfusion is a contributor – but likely not the only one – of the observed dfMRI changes. Similar considerations hold for T_2^* , which role appears limited given the little overlap between dfMRI and GE-BOLD activations.

Analysis of ADC-fMRI voxels where the task paradigm is a significant regressor resulted in bilateral clusters partially overlapping those obtained with GE-BOLD (Figure 3), similarly to what was observed for dfMRI. Activations with ADC-fMRI are generally smaller and noisier than those from dfMRI but show less artefactual areas. Further, the supplementary motor cortex is hardly revealed, which might be partially due to the lower sample size of ADC-fMRI series compared to dfMRI. The ADC-fMRI values increase during activation between 3% (ADC-fMRI^{300}) and 1% (ADC-fMRI^{800} , ADC-fMRI^{1200}), which is in line with what is observed in the visual cortex by Nicolas et al. (Nicolas et al., 2017), and in the same magnitude but opposite sign of what is originally reported by Darquié et al. (Darquié et al., 2001). Considering that $f_{\text{IVIM-fMRI}}$ but not $\text{MD}_{\text{IVIM-fMRI}}$ (Figure 5) shows sensitivity to task execution in $\text{AC}(\text{ADC-fMRI})$, we suggest that the observed increase in ADC values is largely driven by blood volume and T_2 values changes. This result might seem counterintuitive, given the dependency of ADC from T_2 values cancels out in the ADC equation. However, such assumption holds only if the signal originates from a single water pool, i.e., adhering to the classic mono-exponential diffusion equation. When applying the bi-exponential IVIM model, our results indeed show an increase in perfusion signal fraction between 7 and 12% in the ADC-fMRI activations (Supplementary Material Table S2), which is more than what was observed for the dfMRI activations. The activation overlap with $f_{\text{IVIM-fMRI}}$ activations is higher with ADC-fMRI (~22%) than with dfMRI (~15%) (see also Supplementary Figure S2), and $f_{\text{IVIM-fMRI}}$ in $\text{AC}(\text{ADC-fMRI})$ exhibits a stronger correlation with task execution than in $\text{AC}(\text{dfMRI})$. Lastly, changes in ADC-fMRI (Figure 7) show a visible lag to task execution compared to both GE-BOLD and dfMRI (Figure 4), suggesting the latter to be closer to the early activation mechanisms. Given these observations, we conclude that perfusion is likely to be a stronger contributor in the ADC-fMRI response compared to the dfMRI response.

Some limitations of this work must be acknowledged. Our sequence design allows to repeatedly acquire data at multiple diffusion weightings in viable times, allowing to simultaneously derive ADC measures and perfusion signal fractions. However, due to the inherent delay of 7s introduced between the $b = 0 \text{ s/mm}^2$ volume and the last diffusion weighted volume, the temporal resolution advantage of diffusion weighted data at strong b-value might be partially compromised if no further corrections are considered. The perfusion changes observed in this work are noticeably smaller than those reported in Federau et al. (Federau et al., 2015). This might be due to simultaneous mechanisms taking place in the free water regime, which was suppressed with a fluid attenuated inversion recovery acquisition.

Unfortunately, such acquisition is not advantageous in the dfMRI context due to the need for short repetition times. To further investigate such hypothesis, the dfMRI acquisition should be modified to accommodate a third intermediate diffusion weighting value within TR limitations. It is also worth mentioning that in Federau et al. (2015), the value of the TR was 12 times longer than the one used in this study, which affects the T1-weighting of the signal and, hence, may partially explain the observed differences.

The results presented here are in general agreement with recent literature, suggesting potential advantages of dfMRI over GE-BOLD, especially in terms of spatial localization of the brain activated areas. However, it remains unclear whether the more focalized activations detected with dfMRI (and ADC-fMRI) are closer to the real neuronal source of motor activation than conventional fMRI activations, as recently suggested (Nunes et al., 2019). Furthermore, we observed that both dfMRI and ADC-fMRI provide bilateral activations when comparing task and rest conditions, but that the overlap among the two is rather low, suggesting the detection of adjacent but not identical clusters. Establishing which of the two is closer to the neuronal activation will require further investigation, although our results suggest dfMRI as the most likely. From a technological point of view dfMRI, ADC-fMRI and IVIM-fMRI are more challenging to perform than GE-BOLD, they are more prone to artefacts and require more processing steps. Nevertheless, recent advances in hardware will support the applicability of the technique, which complements standard GE-BOLD in providing additional insights into brain activation mechanisms.

Acknowledgements

The research of A.L. is supported by VIDI Grant 639.072.411 from the Netherlands Organisation for Scientific Research (NWO).

References

- Acheson, A., Wijtenburg, S.A., Rowland, L.M., Winkler, A., Mathias, C.W., Hong, L.E., Jahanshad, N., Patel, B., Thompson, P.M., McGuire, S.A., Sherman, P.M., Kochunov, P., Dougherty, D.M., 2017. Reproducibility of tract-based white matter microstructural measures using the ENIGMA-DTI protocol. *Brain Behav.* 7, 1–10. <https://doi.org/10.1002/brb3.615>
- Akhlaghi, H., Corben, L., Georgiou-Karistianis, N., Bradshaw, J., Delatycki, M.B., Storey, E., Egan, G.F., 2012. A functional MRI study of motor dysfunction in Friedreich's ataxia. *Brain Res.* 1471, 138–154. <https://doi.org/10.1016/j.brainres.2012.06.035>
- Aso, T., Urayama, S., Poupon, C., Sawamoto, N., Fukuyama, H., Le Bihan, D., 2009. An intrinsic diffusion response function for analyzing diffusion functional MRI time series. *Neuroimage* 47, 1487–95. <https://doi.org/10.1016/j.neuroimage.2009.05.027>
- Aso, T., Urayama, S.I., Fukuyama, H., Le Bihan, D., 2013. Comparison of diffusion-weighted fMRI and BOLD fMRI responses in a verbal working memory task. *Neuroimage* 67, 25–32. <https://doi.org/10.1016/j.neuroimage.2012.11.005>
- Cho, G.Y., Moy, L., Zhang, J.L., Baete, S., Lattanzi, R., Moccaldi, M., Babb, J.S., Kim, S., Sodickson, D.K., Sigmund, E.E., 2015. Comparison of fitting methods and b-value sampling strategies for intravoxel incoherent motion in breast cancer. *Magn. Reson. Med.* 74, 1077–85. <https://doi.org/10.1002/mrm.25484>
- Dale, A.M., Fischl, B., Sereno, M.I., 1999. Cortical surface-based analysis. I. Segmentation and surface reconstruction. *Neuroimage* 9, 179–94. <https://doi.org/10.1006/nimg.1998.0395>
- Darquié, A., Poline, J.B., Poupon, C., Saint-Jalmes, H., Le Bihan, D., 2001. Transient decrease in water diffusion observed in human occipital cortex during visual stimulation. *Proc. Natl. Acad. Sci. U. S. A.* 98, 9391–5. <https://doi.org/10.1073/pnas.151125698>
- Federau, C., Maeder, P., O'Brien, K., Browaeys, P., Meuli, R., Hagmann, P., 2012. Quantitative Measurement of Brain Perfusion with Intravoxel Incoherent Motion MR Imaging. *Radiology* 265, 874–881. <https://doi.org/10.1148/radiol.12120584>
- Federau, C., O'Brien, K., Birbaumer, A., Meuli, R., Hagmann, P., Maeder, P., 2015. Functional mapping of the human visual cortex with intravoxel incoherent motion MRI. *PLoS One* 10, e0117706. <https://doi.org/10.1371/journal.pone.0117706>
- Finkenstaedt, T., Klarhoefer, M., Eberhardt, C., Becker, A.S., Andreisek, G., Boss, A., Rossi, C., 2017. The IVIM signal in the healthy cerebral gray matter: A play of spherical and non-spherical

- components. *Neuroimage* 152, 340–347. <https://doi.org/10.1016/j.neuroimage.2017.03.004>
- Glover, G.H., 1999. Deconvolution of impulse response in event-related BOLD fMRI. *Neuroimage* 9, 416–29.
- Goense, J.B.M., Logothetis, N.K., 2006. Laminar specificity in monkey V1 using high-resolution SE-fMRI. *Magn. Reson. Imaging* 24, 381–392. <https://doi.org/10.1016/j.mri.2005.12.032>
- Grech-Sollars, M., Hales, P.W., Miyazaki, K., Raschke, F., Rodriguez, D., Wilson, M., Gill, S.K., Banks, T., Saunders, D.E., Clayden, J.D., Gwilliam, M.N., Barrick, T.R., Morgan, P.S., Davies, N.P., Rossiter, J., Auer, D.P., Grundy, R., Leach, M.O., Howe, F.A., Peet, A.C., Clark, C.A., 2015. Multi-centre reproducibility of diffusion MRI parameters for clinical sequences in the brain. *NMR Biomed.* 28, 468–485. <https://doi.org/10.1002/nbm.3269>
- H., C., V.S., L., E., H., B., T., E.E., S., 2011. Comparison of biexponential and monoexponential model of diffusion weighted imaging in evaluation of renal lesions: Preliminary experience. *Invest. Radiol.* 46, 285–291.
- lima, M., Le Bihan, D., 2016. Clinical Intravoxel Incoherent Motion and Diffusion MR Imaging: Past, Present, and Future. *Radiology* 278, 13–32. <https://doi.org/10.1148/radiol.2015150244>
- Jenkinson, M., Bannister, P., Brady, M., Smith, S., 2002. Improved optimization for the robust and accurate linear registration and motion correction of brain images. *Neuroimage* 17, 825–41.
- Jenkinson, M., Beckmann, C.F., Behrens, T.E.J., Woolrich, M.W., Smith, S.M., 2012. FSL. *Neuroimage* 62, 782–90. <https://doi.org/10.1016/j.neuroimage.2011.09.015>
- Keil, V.C., Mädler, B., Gielen, G.H., Pintea, B., Hiththetiya, K., Gaspranova, A.R., Gieseke, J., Simon, M., Schild, H.H., Hadizadeh, D.R., 2017. Intravoxel incoherent motion MRI in the brain: Impact of the fitting model on perfusion fraction and lesion differentiability. *J. Magn. Reson. Imaging* 46, 1187–1199. <https://doi.org/10.1002/jmri.25615>
- Klein, S., Staring, M., Murphy, K., Viergever, M.A., Pluim, J.P.W., 2010. elastix: a toolbox for intensity-based medical image registration. *IEEE Trans. Med. Imaging* 29, 196–205. <https://doi.org/10.1109/TMI.2009.2035616>
- Klein, S., Staring, M., Pluim, J.P.W., 2007. Evaluation of Optimization Methods for Nonrigid Medical Image Registration Using Mutual Information and B-Splines. *IEEE Trans. Image Process.* 16, 2879–2890. <https://doi.org/10.1109/TIP.2007.909412>
- Le Bihan, D., Breton, E., Lallemand, D., Aubin, M.L., Vignaud, J., Laval-Jeantet, M., 1988. Separation of

- diffusion and perfusion in intravoxel incoherent motion MR imaging. *Radiology* 168, 497–505. <https://doi.org/10.1148/radiology.168.2.3393671>
- Le Bihan, D., Urayama, S., Aso, T., Hanakawa, T., Fukuyama, H., 2006. Direct and fast detection of neuronal activation in the human brain with diffusion MRI. *Proc. Natl. Acad. Sci. U. S. A.* 103, 8263–8. <https://doi.org/10.1073/pnas.0600644103>
- Leemans, A., Jeurissen, B., Sijbers, J., Jones, D.K., 2009. ExploreDTI: a graphical toolbox for processing, analyzing, and visualizing diffusion MR data., in: 17th Annual Meeting of the International Society for Magnetic Resonance in Medicine, Honolulu, Hawaii, USA. p. 3537.
- Miller, K.L., Bulte, D.P., Devlin, H., Robson, M.D., Wise, R.G., Woolrich, M.W., Jezzard, P., Behrens, T.E.J., 2007. Evidence for a vascular contribution to diffusion FMRI at high b value. *Proc. Natl. Acad. Sci. U. S. A.* 104, 20967–20972. <https://doi.org/10.1073/pnas.0707257105>
- Nicolas, R., Gros-Dagnac, H., Aubry, F., Celsis, P., 2017. Comparison of BOLD, diffusion-weighted fMRI and ADC-fMRI for stimulation of the primary visual system with a block paradigm. *Magn. Reson. Imaging* 39, 123–131. <https://doi.org/10.1016/j.mri.2017.01.022>
- Nunes, D., Ianus, A., Shemesh, N., 2019. Layer-specific connectivity revealed by diffusion-weighted functional MRI in the rat thalamocortical pathway. *Neuroimage* 184, 646–657. <https://doi.org/10.1016/j.neuroimage.2018.09.050>
- Pasternak, O., Sochen, N., Gur, Y., Intrator, N., Assaf, Y., 2009. Free water elimination and mapping from diffusion MRI. *Magn. Reson. Med.* 62, 717–30. <https://doi.org/10.1002/mrm.22055>
- Pierpaoli, C., Jones, D.K., 2004. Removing CSF Contamination in Brain DT-MRIs by Using a Two-Compartment Tensor Model C., in: International Society for Magnetic Resonance in Medicine. p. Kyoto, Japan.
- Provenzale, J.M., Engelter, S.T., Petrella, J.R., Smith, J.S., MacFall, J.R., 1999. Use of MR exponential diffusion-weighted images to eradicate T2 “shine-through” effect. *AJR. Am. J. Roentgenol.* 172, 537–9. <https://doi.org/10.2214/ajr.172.2.9930819>
- Rudrapatna, U.S., van der Toorn, A., van Meer, M.P.A., Dijkhuizen, R.M., 2012. Impact of hemodynamic effects on diffusion-weighted fMRI signals. *Neuroimage* 61, 106–14. <https://doi.org/10.1016/j.neuroimage.2012.02.050>
- Setsompop, K., Gagoski, B.A., Polimeni, J.R., Witzel, T., Wedeen, V.J., Wald, L.L., 2012. Blipped-controlled aliasing in parallel imaging for simultaneous multislice echo planar imaging with reduced g-factor penalty. *Magn. Reson. Med.* 67, 1210–1224.

<https://doi.org/10.1002/mrm.23097>

Sigmund, E.E., Vivier, P.-H., Sui, D., Lamparello, N. a., Tantillo, K., Mikheev, a., Rusinek, H., Babb, J.S., Storey, P., Lee, V.S., Chandarana, H., 2012. Intravoxel Incoherent Motion and Diffusion-Tensor Imaging in Renal Tissue under Hydration and Furosemide Flow Challenges. *Radiology* 263, 758–769. <https://doi.org/10.1148/radiol.12111327>

Smith, S.M., 2002. Fast robust automated brain extraction. *Hum. Brain Mapp.* 17, 143–55. <https://doi.org/10.1002/hbm.10062>

Song, A.W., Woldorff, M.G., Gangstead, S., Mangun, G.R., McCarthy, G., 2002. Enhanced spatial localization of neuronal activation using simultaneous apparent-diffusion-coefficient and blood-oxygenation functional magnetic resonance imaging. *Neuroimage* 17, 742–50. [https://doi.org/10.1016/S1053-8119\(02\)91217-6](https://doi.org/10.1016/S1053-8119(02)91217-6)

Williams, R.J., McMahon, K.L., Hocking, J., Reutens, D.C., 2014. Comparison of block and event-related experimental designs in diffusion-weighted functional MRI. *J. Magn. Reson. Imaging* 40, 367–375. <https://doi.org/10.1002/jmri.24353>

Winston, G.P., 2012. The physical and biological basis of quantitative parameters derived from diffusion MRI. *Quant. Imaging Med. Surg.* 2, 254–65. <https://doi.org/10.3978/j.issn.2223-4292.2012.12.05>

Supplementary Material

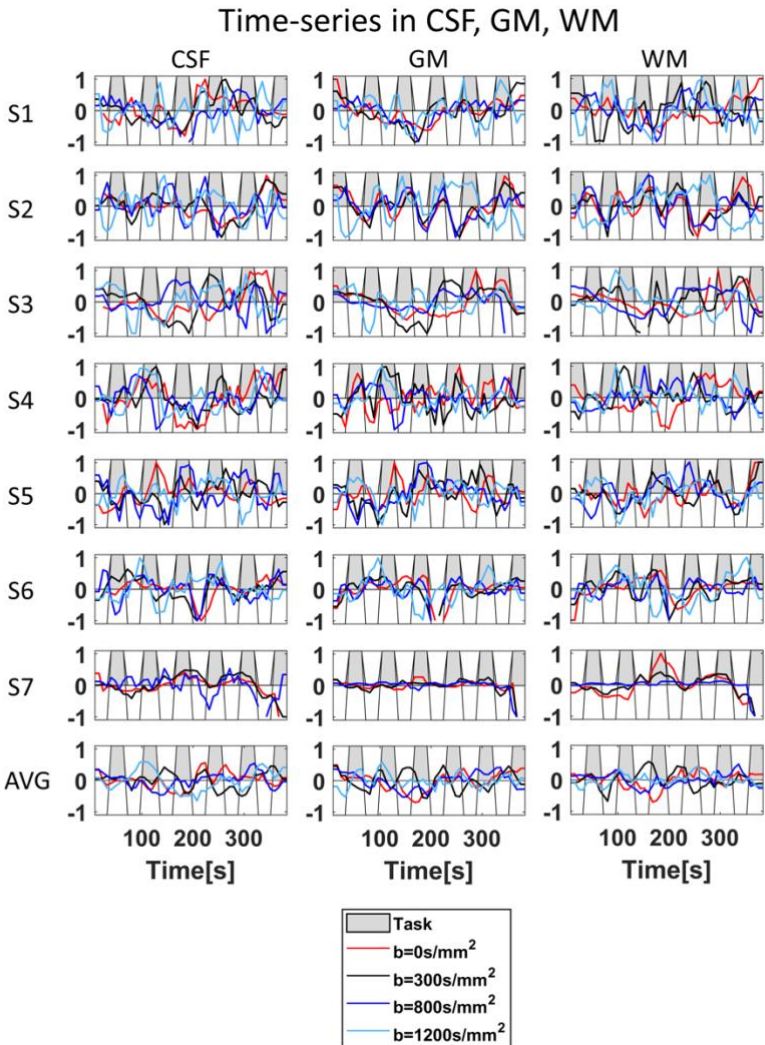


Figure S1: dfMRI time-series in CSF, GM, WM. Normalized average time-series of Z(dfMRI) for each diffusion weighting (red, black, blue and light blue solid lines) in the CSF, GM and WM of each subject (each row). The applied stimuli are shown in background as grey (task) and white (rest) blocks. No patterns were observed between task execution and time-series changes.

| Time-series | Change (%) | p-value |
|---|-------------|--------------------|
| AC(dfMRI) | | |
| b = 0 s/mm ² [1] | 0.64 ± 0.23 | 2×10 ⁻⁴ |
| b = 0 s/mm ² [2] | 0.69 ± 0.23 | 8×10 ⁻⁴ |
| b = 300 s/mm ² [1] | 0.35 ± 0.17 | 2×10 ⁻³ |
| b = 300 s/mm ² [2] | 0.37 ± 0.16 | 2×10 ⁻³ |
| b = 800 s/mm ² | 0.35 ± 0.13 | 1×10 ⁻³ |
| b = 1200 s/mm ² | 0.53 ± 0.24 | 3×10 ⁻³ |
| f _{IVIM} -fMRI ³⁰⁰⁻⁸⁰⁰ | 4.89 ± 1.95 | 6×10 ⁻⁴ |
| f _{IVIM} -fMRI ³⁰⁰⁻¹²⁰⁰ | 4.64 ± 2.20 | 9×10 ⁻³ |
| MD _{IVIM} -fMRI ³⁰⁰⁻⁸⁰⁰ | 0.37 ± 0.13 | 1×10 ⁻³ |
| MD _{IVIM} -fMRI ³⁰⁰⁻⁸⁰⁰ | 0.66 ± 0.66 | 6×10 ⁻² |

Table S1: Average ± standard deviation of dfMRI, f_{IVIM}-fMRI and MD_{IVIM}-fMRI changes between task and rest condition within AC(dfMRI). [1] and [2] refer to the first and the second dfMRI acquisition, respectively. The p-value refers to a two sided t-test between the average values in the two conditions.

| AC(ADC-fMRI) | | |
|--|--------------|--------------------|
| ADC-fMRI ³⁰⁰ [1] | 3.26 ± 1.88 | 4×10 ⁻³ |
| ADC-fMRI ³⁰⁰ [2] | 3.08 ± 1.48 | 4×10 ⁻³ |
| ADC-fMRI ⁸⁰⁰ | 1.23 ± 0.58 | 4×10 ⁻³ |
| ADC-fMRI ¹²⁰⁰ | 1.50 ± 0.91 | 1×10 ⁻² |
| f _{IVIM} -fMRI ³⁰⁰⁻⁸⁰⁰ | 12.33 ± 8.26 | 8×10 ⁻³ |
| f _{IVIM} -fMRI ³⁰⁰⁻¹²⁰⁰ | 7.52 ± 4.13 | 7×10 ⁻³ |
| MD _{IVIM} -fMRI ³⁰⁰⁻⁸⁰⁰ | 0.68 ± 0.48 | 1×10 ⁻² |
| MD _{IVIM} -fMRI ³⁰⁰⁻¹²⁰⁰ | 0.74 ± 0.54 | 2×10 ⁻² |

Table S2: Average ± standard deviation of ADC-fMRI, f_{IVIM}-fMRI and MD_{IVIM}-fMRI changes between task and rest condition within AC(ADC-fMRI). [1] and [2] refer to the first and the second dfMRI acquisition, respectively. The p-value refers to a two sided t-test between the average values in the two conditions.

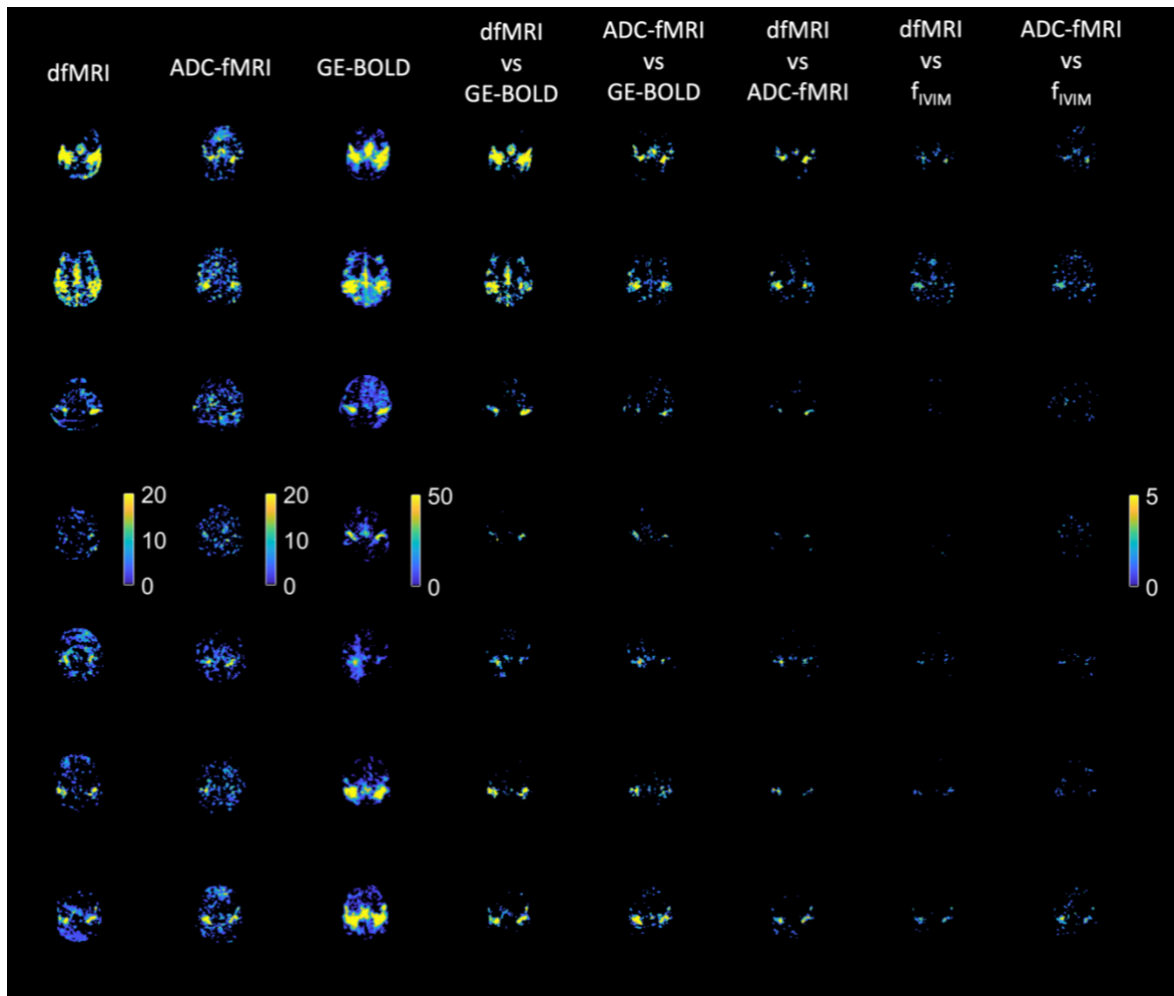


Figure S2: Axial projection of the significant Z-scores derived with dfMRI, ADC-fMRI, GE-BOLD (columns 1-3), and of their overlaps (columns 4-8). GE-BOLD resulted in the largest activation areas, followed by dfMRI and ADC-fMRI. Activations computed with ADC-fMRI visually had slightly larger overlap with f_{IVIM} than those computed with dfMRI.